Solid lubrication performance of hybrid Ti3C2Tx/MoS2 coatings

Solid Lubrication Performance of Hybrid $Ti_3C_2T_x/MoS_2$ Coatings

Guido Boidi[1], Dario Zambrano[2], Sabine Schwarz[3], Edoardo Marquis[4], Markus Varga[1], Manel Rodríguez Ripoll[1], Ewald Badisch[1], Maria Clelia Righi[4], Carsten Gachot[5], Philipp G. Grützmacher[5] and Andreas Rosenkranz[2]*

[1] AC2T research GmbH, Viktor-Kaplan-Straße 2/C, Wiener Neustadt 2700, Austria
[2] Department of Chemical Engineering, Biotechnology and Materials, FCFM, University of Chile, Santiago 8370415, Chile
[3] USTEM, TU Wien, Wiedner Hauptstraße 8-10, Vienna 1040, Austria
[4] Department of Physics and Astronomy "Augusto Righi", University of Bologna, Bologna 40127, Italy
[5] Department of Engineering Design and Product Development, TU Wien, Wien 1060, Austria

***Corresponding Authors**
Email: Prof. Dr. Andreas Rosenkranz, arosenkranz@ing.uchile.cl

Abstract

MXenes have gained notable attention in tribology due to their excellent wear resistance based on the formation of beneficial tribofilms. However, studies using MXenes as solid lubricants have mainly focused on multi-layer $Ti_3C_2T_x$ coatings, while little is known about the tribological performance of MXene composites. Therefore, our study aims at scrutinizing and understanding the tribological behavior of MXenes and MXene composites as solid lubricants under reciprocating sliding conditions. Theoretical predictions regarding the resulting interlayer adhesion and coating-substrate adhesion helped to design the hybrid coatings. Multi-layer $Ti_3C_2T_x$, molybdenum disulfide (MoS_2) and two hybrid coatings using $Ti_3C_2T_x$ and MoS_2 (random mixture and sandwich-like) were spray-coated onto steel substrates with a coating thickness of about 800 nm. Dry sliding tests using a steel ball as counter-body were carried out at room temperature. The coatings' morphology and formed tribofilms were holistically characterized by scanning and transmission electron microscopy (SEM, TEM) as well as X-ray photoelectron spectroscopy (XPS). Our results demonstrate that both hybrid coatings notably reduce friction and wear, outperforming their respective pure coatings ($Ti_3C_2T_x$ and MoS_2). This is attributed to synergistic effects between $Ti_3C_2T_x$ and MoS_2, with adhesion forces appearing to be the governing mechanism in enhancing the formation of stable tribofilms. Numerical calculations validate our experimental results, verifying that hybrid coatings exhibit low interlayer friction and high adhesion to ferrous substrates. Consequently, our work reveals the potential of $Ti_3C_2T_x/MoS_2$ hybrid coatings to further optimize friction and wear.

Keywords:
2D materials; $Ti_3C_2T_x$; MoS_2; solid lubrication; composite coatings; tribofilm formation

1. INTRODUCTION

The current environmental scenario demands effective tribological solutions to reduce pollutant emissions and improve systems' efficiency by reducing friction and wear [1,2]. The strategy of using low-viscosity lubricants approaches its limits, since it goes hand in hand with reduced lubricant thicknesses, thus increasing the probability of asperity contact, friction, and wear. Therefore, researchers strive to find alternative strategies to improve the tribological behavior under mixed and boundary lubrication by applying solid lubricants. A class of solid lubricants intensively researched for their outstanding properties are 2D materials [3–5].

In the last two decades, 2D materials showcased their outstanding mechanical, electrical, and thermal properties compared to their 3D precursor materials [6–8]. Layered 2D materials can form easy-to-shear tribolayers, which separate both rubbing surfaces, thus reducing friction and wear [9–11]. In this regard, graphene and transition metal dichalcogenides (TMDs) are the most studied 2D materials until now [12,13]. However, since their discovery in 2011, the more recently established material class of MXenes has rapidly gained notable attention owing to their tunable structure and chemistry, offering tremendous potential for tribological applications [14,15].

MXenes are early transition metal carbides, nitrides, or carbonitrides, which are synthetized from MAX-phase precursors by selectively removing their A layers [14,16]. MXenes' general formula is $M_{n+1}X_nT_x$ (n between 1 and 4, with M being an early transition metal and X either C or N, while T_x represent all surface terminations, e.g., –O, –Cl, –F or –OH [14]. The combination of possible chemical elements and surface terminations permits to tune MXenes' properties, thus making them more versatile than traditional 2D materials. Despite their already observed excellent properties, it is anticipated that MXenes' true potential is yet to be explored [17].

Applications such as energy storage/harvesting and electromagnetic shielding have been initially studied [18–20], whereas tribological and mechanical properties have moved to the focus of research only in the past 5 years [3,21,22]. Even though there is a vast variety of possible MXenes, multi-layer $Ti_3C_2T_x$ is by far the most studied in tribology [17,21]. In this context, MXenes can be either used as lubricant additives [23,24], solid lubricants [25,26], or fillers in composites [27,28]. MXenes and, particularly multi-layer $Ti_3C_2T_x$, have shown an excellent wear resistance [29] and friction reduction (coefficient of friction (COF) ≈ 0.1 - 0.3 under dry sliding conditions and low relative humidities) [30] in particular when used as solid lubricants deposited on various substrates by spray-coating, drop casting or electro-spraying [29,31,32]. The observed experimental tendencies were traced back to the formation of a stable tribofilm [33]. Generally, it has been found that homogenous, high-quality coatings are required for an excellent tribological performance. Additionally, irrespective of the deposition technique, the establishment of a proper substrate-coating interface is crucial for achieving superior tribological performance under solid lubrication [17]. In this regard, recent experimental and computational studies focused on the adhesion forces between MXenes with homogeneous and mixed terminations to better understand their tribological properties [34–36]. It has been demonstrated that MXenes' surface terminations significantly influence their interlayer and substrate adhesion, thus greatly affecting the resulting tribological performance. The best combination of low interlayer binding and high adhesion to ferrous substrates was verified for -O terminations, whereas -OH groups increased interlayer binding and -F groups reduced the resulting substrate adhesion. In contrast, the monolayer thickness (Ti_2CT_x versus $Ti_4C_3T_x$) was shown to have a marginal effect on adhesion [36].

Based on the presented state-of-the-art, it becomes evident that 2D materials and, particularly, MXenes can notably improve the performance of tribological components. Little knowledge is

available about MXenes' true tribological potential, since a systematic study evaluating the effect of different tribological loading conditions is still missing. Moreover, only few studies have combined $Ti_3C_2T_x$ with other 2D materials (e.g., graphene or MoS_2) to induce synergistic tribological effects [37–39].

Therefore, our work aims at studying the tribological performance of $Ti_3C_2T_x$ and $Ti_3C_2T_x/MoS_2$ hybrid coatings used as solid lubricants under reciprocating sliding conditions. Uncoated ball bearing steel substrates were used as benchmark references, while the tribological performance of pure $Ti_3C_2T_x$ and MoS_2 coatings was also addressed. An in-depth post-mortem characterization of the wear tracks helped to shed light on the underlying mechanisms responsible for the observed tribological phenomena. The experimental work was complemented with density functional theory (DFT) simulations used for determining the interlayer adhesion between MoS_2 and MXene, as well as their respective adhesion onto ferrous substrates (i.e., pure iron and hematite).

2. MATERIALS AND METHODS

2.1 Materials and coating deposition

Ball bearing steel (AISI 52100) was used for both tribological counter-bodies of the reciprocating ball-on-disc test, namely, disc Ø24 ×7.9 mm (Ra = 35 nm) and ball Ø10 mm (Ra = 20 nm - grade G10). The solid lubricant coatings were applied on the plane surface of the discs by spray-coating. As subsequently explained, a user-developed spray routine has been developed to enhance coating uniformity. Uncoated discs and balls were tested as reference material.

As coating materials, multi-layer $Ti_3C_2T_x$ and molybdenum disulphide (MoS_2) nano-sheets were utilized. For sake of simplicity, multi-layer $Ti_3C_2T_x$ will be just named **MXene** throughout the entire manuscript. Regarding MXenes' synthesis, commercial Ti_3AlC_2 MAX-powder (FORSMAN SCIENTIFIC Co. Ltd., Beijing, China) was immersed in a 40 % hydrofluoric acid solution. Under continuous stirring at room temperature for two hours, the reaction product was neutralized by several washing cycles with deionized water. Using centrifugation, the powder was separated prior to filtering under vacuum conditions and freeze-drying. The described synthesis resulted in multi-layer MXenes with a negligible amount of aluminum having x-y dimensions of about 2-3 μm. In z-direction, the as-fabricated multi-layers consisted of about 100-120 layers, thus being around 100 nm thick (0.9 nm average layer distance) (**Figure S1a**). More details about the synthesis process and the physicochemical characteristics of the as-synthesized MXenes can be found in **Figure S1** in the Supporting Information and previously published research works [23,29,31,40]. Commercial MoS_2 powder was purchased from Graphene supermarket (United States). In this regard, the MoS_2 powder demonstrated a multi-layer structure with an interlamellar spacing of about 0.58 nm as measured by high-resolution transmission electron microscopy (**Figure S1b)**. The initial characterization of MXene and MoS_2 powders were conducted via

Raman spectroscopy (LabRAM HR Evolution). Raman spectra were obtained in backscattering geometry using a laser excitation wavelength of 532 nm. The laser output was 105 mW at the source and ~2 mW at the sample. The spectra were recorded in the spectral range from 80 to 1000 cm^{-1} with an acquisition time of 128 s/spectrum and a spectral resolution of 3 cm^{-1} using a grating with a resolution of 1800 grooves/mm.

In general, four different coating systems were fabricated: a MXene coating, a MoS_2 coating, and two hybrid coatings consisting of a mixture of MXenes and MoS_2 (**Table 1**). Irrespective of their composition, the 2D materials were mixed with ethanol using a concentration of 2 mg/ml. Composite I was prepared by dispersing MXenes and MoS_2 in ethanol in the same weight fraction. The dispersions were homogenized for 5 minutes at 10,000 rpm using a shear-mixer (HG-15D digital homogenizer - Daihan Scientific). The dispersion and distribution of the nano-sheets were improved using tip sonication (QSONICA CL-18 Sonicators) for 1 hour (sonication time 5 s on, 5 s off, 50 W power), followed by 2 hours of bath sonication. Afterwards, the solution was spray-coated on the steel disc samples: The samples were arranged on a heating plate maintained at 75°C during spray-coating to speed up the solvent evaporation. A nozzle-substrate distance of 100 mm was kept constant for all samples. A pressure of 20 psi (1.38 bar) in the compressor was used during spray-coating.

Composite II was produced by creating a sandwich-like structure with MXene being the bottom and MoS_2 being the top layer as illustrated in **Table 1**. The sprayed volume was adjusted to obtain a coating thickness of 800 nm for all coatings (Composite I had two layers with an individual thickness of about 400 nm) except for MXene, which had a coating thickness of about 300 nm**.** After initial tribological pre-tests, it was observed that an increased MXene thickness brought drawbacks when compared to thinner coatings. Similar results had also been previously published

[26,41]. The resulting coating thicknesses were measured using white light interferometry (WLI, MFT-500, Rtec Instruments).

Table 1. Summary of deposited coatings including coating design, thickness, deposited volume, and schematic representation of all samples considered.

Name	Material / Coating	Volume sprayed (ml)	Coating thickness (nm)	Schematic
REF	Ball bearing steel AISI 52100	/	/	
MXene	MXene multi-layer $Ti_3C_2T_x$	2	275 ± 25	
MoS_2	Molybdenum disulphide	4	775 ± 35	
Composite I	"Mix": MXene (50%) + MoS_2 (50%)	6	825 ± 55	
Composite II	"Bilayer": MXene bottom + MoS_2 top	8 (4+4)	850 ± 50	

2.2 Tribological testing and tribofilm characterization

The tribological experiments were carried out under reciprocating sliding using an SRV®5 tribometer from Optimol Instruments. The disc samples were fixed on at the bottom part of the tribometer, whereas the balls are mounted on the upper oscillating sample holder. An electrical linear motor controls the frequency and stroke of the ball, while the normal load was applied to the disc through a load cell. Two piezo electric force sensors mounted on the disc sample holder measured the vertical (load) and lateral (frictional) forces (**Figure S2**).

The samples were tested at a Hertzian contact pressure of 0.8 GPa, an oscillating frequency of 1 Hz, a stroke length of 2.5 mm, and a testing time of 15 minutes. The selection of the tribological conditions was backed upon previous research conducted by the authors, in which MXene solid lubricant coatings showed a beneficial friction evaluation up to contact pressures of 0.5 GPa [26]. A higher load has been selected in our study (contact pressure of 0.8 GPa) to verify MXenes' operational limits and evaluate the potential of hybrid coatings for severe operations. The tests were performed at room temperature (20°C) and a relative humidity of 40 %. Each testing condition was repeated three times for statistical reasons to calculate mean values and standard deviations.

The wear tracks were analyzed post-mortem by scanning electron microscopy (SEM, multi beam system JIB-4700F – JEOL) with energy-dispersive X-ray spectroscopy (EDS), focused ion beam microscopy (FIB), X-ray photoelectron spectroscopy (XPS) and transmission electron microscopy (TEM, FEI TECNAI F20). XPS maps were acquired using a Thermo Fisher Scientific Thetaprobe with a monochromatic Al K_α X-ray source (1486.6 eV). The pass energy of 200 eV and spectrum energy step size of approximately 0.7 eV were used. The X-ray spot on the sample surface had a diameter of 50 µm and the map grid step size was likewise set to 50 µm. Prior to analysis, the whole map area was briefly sputter-cleaned with 3 keV Ar ions. Peak fitting was carried out with the Thermo Fisher Scientific Avantage Data System software using Gaussian/Lorentzian functions for peak fitting. The C_{1s} peak of adventitious carbon located at 284.8 eV was utilized as a binding energy reference.

For TEM investigation, the lamellae were prepared by FIB. The TEM lamellae had a size of ~30×10 μm^2, with a thickness of <100 nm at the areas of interest (near the surface layer). TEM-EDS mappings and line-scans provided information on the chemical composition. High Angle

Annular Dark Field (HAADF) images showed elemental Z-contrast, while TEM imaging revealed the structure of the formed tribofilms. Additionally, Selected Area Electron Diffraction (SAED) patterns were used for phase analysis. Additional high resolution-TEM (HR-TEM) imaging was performed for phase analysis using Fourier Transformation (FT) and the measurements of lattice spacings in the HR-TEM images.

2.3 Numerical simulation

The adhesion of pure MoS_2 and MXene layers onto steel substrates and the interlayer adhesion between MoS_2 and MXene layers were numerically evaluated using density functional theory (DFT) calculations to support coating design and improve the interpretation of the underlying mechanisms responsible for the experimental results. Previous numerical results proved that the MXene monolayer thickness plays a marginal role in terms of adhesion [36]. In our previous work, the work of separation and adhesion forces of Ti_2C, Ti_3C_2 and Ti_4C_3 MXenes have been shown to be mainly influenced by their surface termination rather than the monolayer thickness and overall stoichiometry [36]. Therefore, Ti_2CT_x layers were simulated to reduce computational effort.

Spin-polarized DFT calculations were carried out as implemented in version 7.2 of the Quantum ESPRESSO package. The Perdew-Burke-Ernzerhof (PBE) parametrization within the general gradient approximation (GGA) approach was adopted for the description of the exchange and correlation functional. A dispersion term (DFT-$D2_{NG}$) was incorporated for the inclusion of van der Waals interactions. The $D2_{NG}$ scheme is a modification of the Grimme-D2 parametrization, in which the C_6 and R_0 coefficients of the metal atoms (Ti, Mo, and Fe) are replaced with those of the preceding noble gas (i.e., Ar). The authors have already tested the accuracy of the $D2_{NG}$ scheme in the past [36], revealing its ability to accurately improve the description of the interlayer

interaction between MXenes. The electronic wave-functions were expanded on a plane-waves basis truncated with a cut-off of 50 Ry, while a cut-off of 400 Ry was employed for the charge density, accordingly to our previous studies on MXenes [36,42]. The ionic species were described by ultra-soft pseudopotentials with 4 (C), 6 (O and S), 7 (F), 12 (Ti), 14 (Mo), and 16 (Fe) explicit electrons. Default thresholds on the total energy (10^{-4} Ry) and forces (10^{-3} Ry/Bohr) were used for structural optimizations, while adopting a Gaussian smearing of 0.02 Ry for the electronic state occupation around the Fermi level.

To avoid spurious vertical interactions between replicated images, 15 Å of vacuum were included along the axis perpendicular to the surfaces. Ti_2CT_x@MoS_2 and Ti_2CT_x@Fe_2O_3 bilayers were modelled using hexagonal cells of size 9.32 and 9.97 Å, respectively. The mismatch between the equilibrium lattice parameter of the hetero-interfaces and that of their constituents never exceeded 5%. Please note that the Ti_2CT_x layers contained a mixture of terminations, which is representative of the realistic conditions [43]. Therefore, the stoichiometric formula of our MXene model is $Ti_2C(F_{1/3}O_{1/3}OH_{1/3})_2$, but for simplicity we will refer to it as Ti_2CT_x. The Brillouin zone of the hexagonal cells was sampled with a 6×6×1 Monkhorst−Pack grid for Ti_2CT_x@MoS_2, and a 3×3×1 grid for Ti_2CT_x@Fe_2O_3, respectively, ensuring the convergence of the total energy. The hematite surface (Fe_2O_3) was modelled with the Fe-terminated (001) plane, being one of the dominating planes in most of natural conditions[44]. The PBE functional with the inclusion of the Hubbard correction (PBE-$D2_{NG}$+U) was used for both the Fe_2O_3 surface and the Ti_2CT_x@Fe_2O_3 interface to compensate the onsite repulsion between d electrons of iron. In fact, Fe_2O_3 is a strongly correlated system with the wave function showing an antiferromagnetic character. The value of the *U* parameter was set to 4.2 eV, as described and explained in our previous work [36].

The work of separation, which is the opposite of the adhesion energy, was calculated as a difference between the total energy of the single surfaces ($E_1 + E_2$) and the total energy of the corresponding interface (E_{12}), divided by the in-plane area of the cell:

$$W_{SEP} = \frac{(E_1 + E_2) - E_{12}}{A_{cell}} \quad (1)$$

From this equation, the higher the W_{SEP} values, the greater the interlayer and layer-substrate interactions. The work of separation changes as a function of the relative lateral position of the interface constituents. Therefore, we evaluated the interlayer and layer-substrate adhesion sampling different inequivalent lateral positions. The W_{SEP} values presented in this manuscript refer to the thermodynamically most favorable lateral position between adjacent layers.

We would like to point out that the numerical simulations were not intended to replicate the entire complex tribological system. Therefore, aspects including plastic deformation, atomic mixing, chemical reactions, and structural transformations have not been considered in this contribution. Consequently, our simulations focused on the adhesion between 2D interlayers and substrate, giving fundamental insights and guidance for the design of the targeted composite coatings. Additionally, together with the detailed post-mortem analysis of the contact surfaces, the numerical simulation supported the interpretation of the complex mechanisms between the rubbing surfaces during tribo-testing.

3. RESULTS AND DISCUSSION

3.1 Theoretically predicted adhesion behavior

It is well accepted that the tribological performance of 2D materials is greatly influenced by their interlayer adhesion (between adjacent layers) and the resulting coating-substrate adhesion [36]. To

shed light on both aspects from a theoretical point of view, we calculated the work of separation W_{SEP} between the 2D materials and with the ferrous substrate, i.e., iron (011) and iron oxide (001), which can give useful indications regarding the resulting coating design.

Concerning the work of separation of the coating-substrate interface, pure MoS_2 adheres better to pure iron (1.30 J/m^2) than Ti_2CT_x (0.40 J/m^2) as shown in **Figure 1a.** When considering iron oxide Fe_2O_3, the opposite trend can be recognized since Ti_2CT_x shows an increased W_{SEP} (0.87 J/m^2) compared to MoS_2 (0.35 J/m^2). This can be related to both charge- and hydrogen-transfer from the MXene layer to the hematite surface. The formation of chemical bonds between MXene' terminations and the exposed Fe atoms of Fe_2O_3, as well as the H-transfer from the hydroxyl groups of Ti_2CT_x to the oxygen atoms of the hematite can be seen in **Figure 1b**. Since the used substrate is covered by a thin native oxide layer, these numerical insights motivate the usage of a MXene bottom layer in a sandwich-layer structure with MoS_2 being the top-most layer.

With respect to the interlayer adhesion, it is important to point out that a lower W_{SEP} between the 2D layers indicates an improved lubricity. The interlayer adhesion between pure MoS_2 layers is 0.27 J/m^2, which explains the generally excellent lubricating capability of this material. Interestingly, the interlayer adhesion between MoS_2 and Ti_2CT_x with 0.25 J/m^2 has been estimated to be very similar, which indicates a similarly excellent lubricity for these hetero-interfaces. In contrast, the inherent adhesion between adjacent Ti_2CT_x layers is significantly higher (0.52 J/m^2). Since the resistance to sliding typically decreases with the interfacial adhesion[45], coatings composed of a mixture of MoS_2 and MXenes are highly promising to improve the frictional performance. Therefore, the theoretical calculations are indicative that MXene/MoS_2 composites can offer low interlayer friction and high adhesion to ferrous substrates, which may lead to an excellent frictional performance, thus outperforming pure MXene and MoS_2 coatings.

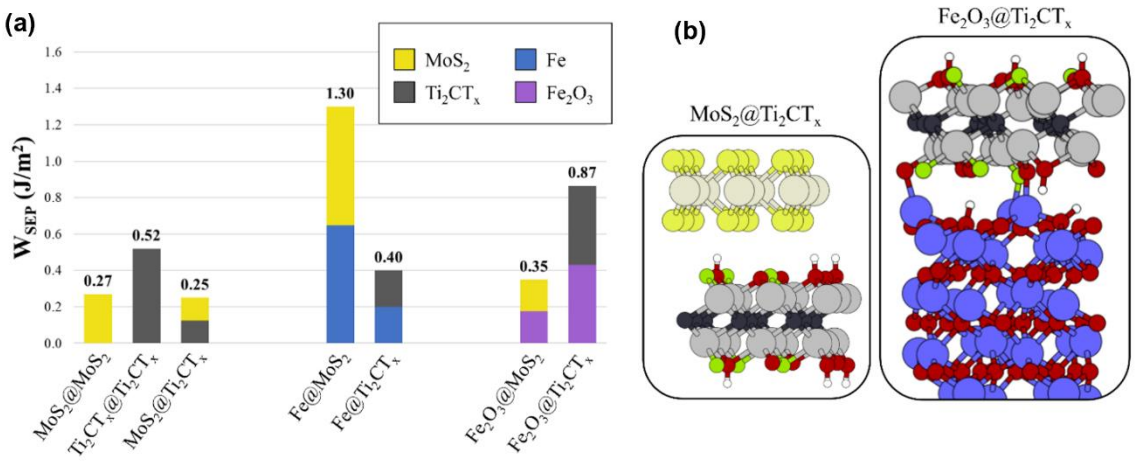

Figure 1. (a) Work of separation (W_{SEP}) for MoS_2/MoS_2, MoS_2/Ti_2CT_x and Ti_2CT_x/Ti_2CT_x interfaces (left-hand side) as well as MoS_2 and Ti_2CT_x onto pure iron (middle) and (0001) hematite surfaces (right-hand side), respectively. (b) Optimized configuration for the $MoS_2@Ti_2CT_x$ bilayer and the Ti_2CT_x layer interacting with Fe_2O_3, respectively.

3.2 Structure, morphology, and surface chemistry of the as-deposited coatings

Using SEM, the cross-sectional morphology of the as-prepared hybrid coatings was assessed (**Figure 2**). Due to the contrast with the underlying steel substrates, coatings with homogenous thicknesses can be clearly distinguished. Within the coatings, contrast differences become noticeable in the HAADF images, for which MXene-rich areas tend to be darker, while zones enriched in MoS_2 appear brighter (**Figure 2a** and **b**). The corresponding elemental mappings (**Figure 2c** and **d**) and EDS line-scans (**Figure 2e** and **f** as indicated in **Figure 2a** and **b**) verify the success of the adopted approach. For Composite I, MXene (Ti signal in yellow) and MoS_2 (Mo signal in red) are randomly intermixed, while larger MXene flakes are surrounded by smaller MoS_2 particles. In the case of Composite II, MXene can be identified as the bottom-layer, while MoS_2 is the top-layer. This is also well reflected by the EDS line-scans, showing alternating S (from MoS_2) and Ti (from MXene) signals for Composite I and a clear separation between S and Ti signals for Composite II. The fact that the bottom MXene layer in Composite II is not perfectly continuous

can be traced back to spray-coating, in which the nanomaterials are stochastically deposited on the substrate.

Apart from the overall morphology and coating structure, the surface chemistry of all as-deposited coatings was assessed by XPS (**Figure S3** for the pure $Ti_3C_2T_x$ and MoS_2 coatings as well as **Figure S4** for both hybrid composites). In the case of the as-deposited $Ti_3C_2T_x$ coating, three different peak regions, namely the C_{1s}, Ti_{2p} and O_{1s} regions, were considered (**Figure S3a-c**). Regarding the analysis of the C_{1s} peak (**Figure S3a**), three contributions located at 284.8, 286.1 and 288.8 eV were detected, which can be assigned to C-C, C-O and C=O bonds, respectively (presence of organic components) [46–49]. The peak fitting of the Ti_{2p} region (**Figure S3b**) required four doublets. The major doublet (458.7 and 464.4 eV) is associated with superficial titanium dioxide, while the other doublets represent Ti-C (454.3 and 460.0 eV), TiC_x/TiC_xO_y (456.0 and 461.7 eV) and, TiO_2; $TiO_{2-X}F_{2X}$ bonds (457.2 and 462.9 eV) [46–48]. The fit functions necessary to describe the observed contributions for the O_{1s} peak can be assigned to metal oxides (Ti (IV) bonding states) as well as C-O and C=O bonds [46–48]. A summary of all fitted XPS data for the as-deposited pure $Ti_3C_2T_x$ coating including the BEs, FWHMs, peak areas, relative atomic percentage (at.-%), and the respective assignment can be found in **Table S1**.

Concerning the as-deposited MoS_2 coating, the respective analysis is shown in **Figure S3d-f** and summarized in **Table S2**. The high-resolution analysis of the Mo_{3d} and S_{2s} peak regions (**Figure S3d-e**) reveal the presence of two doublets each, for which their main contribution located at 229.8 (233.0 eV) for Mo_{3d} and 162.4 (163.9 eV) for Mo_{3d} and S_{2s}, respectively correspond to MoS_2 [50–52]. The other doublet detected for the Mo_{3d} peak at 233.2 (236.2 eV) connects with MoO_3, whereas another contribution for Mo_{3d} at 226.8 eV is assigned to sulfate species [50,51]. MoO_3,

sulfates, organic compounds (SO_4^{2-}/C-O/C=O) and absorbed water can be assigned to the respective contributions found in the O_{1s} peak [46,48–51].

With regard to Composite I (mixed hybrid coating), a detailed HR-XPS analysis was performed for the main S_{2p}, Mo_{3d}, Ti_{2p}, and O_{1s} peaks as shown in **Figure S4a-d** and summarized in **Table S3**. Similar contributions with slightly changed relative intensities were found as for the as-deposited pure $Ti_3C_2T_x$ and MoS_2 coatings. Related to Composite II (bilayer hybrid coating), the HR-XPS analysis was conducted for the S_{2p}, Mo_{3d}, Ti_{2p}, and O_{1s} peak regions as depicted in **Figure S4e-h** and summarized in **Table S4**. As verified in **Figure S4g,** no Ti signal was observed. Moreover, the S, Mo, and O signals appear similar than the signals for pure MoS_2 coating. For both hybrid coatings, an increased amount of sulfate species has been detected. In this regard, the environmental exposure of nano-MoS_2 may help to promote its oxidation, which induces the formation of Mo (V), Mo (VI), and sulfate species. The respective sulfate species may be present as free sulfuric acid and/or coordinating sulfates in Mo−O−S moieties [53]. We anticipate that the underlying oxidation kinetics of MoS_2 may have been accelerated by the heating during spray-coating. However, the HR-XPS analysis aligns well with the conducted SEM analysis thus confirming the successful fabrication of the pure and hybrid coatings.

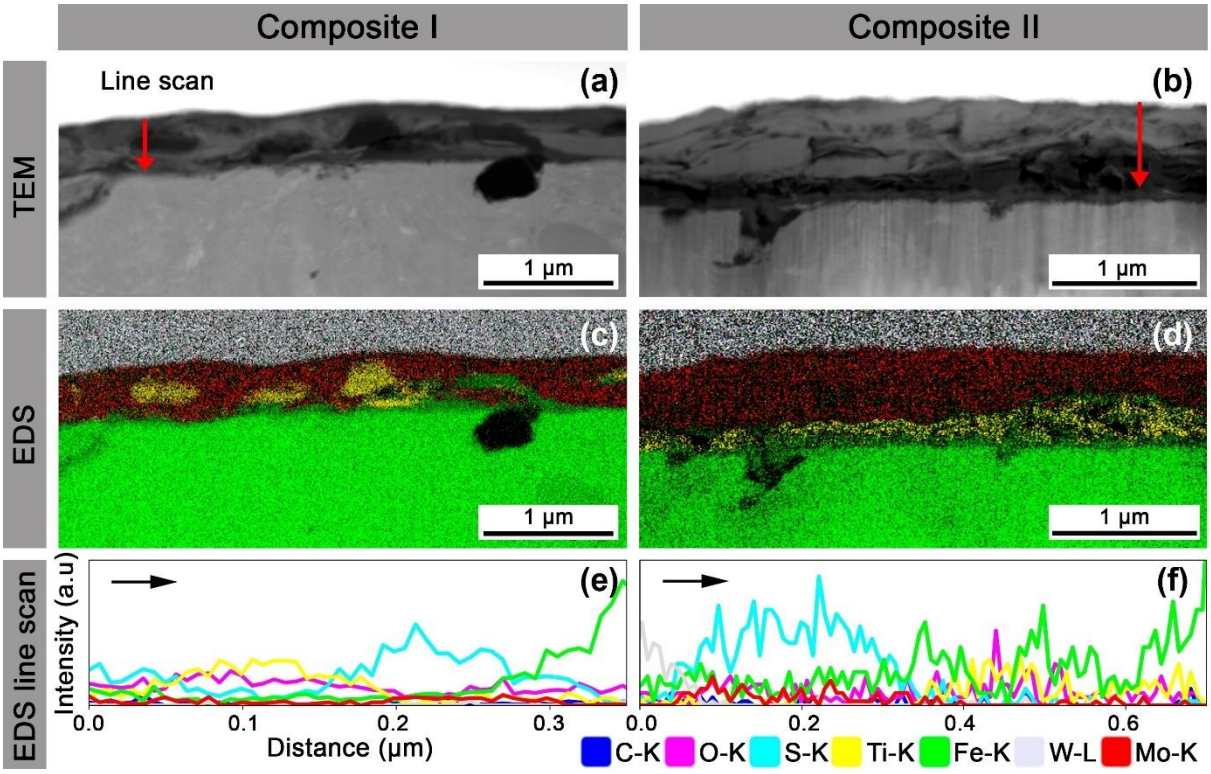

Figure 2. Cross-sectional morphology of the as-sprayed (a) Composite I and (b) Composite II coatings as analyzed by transmission electron microscopy. (a) and (b) demonstrate cross-sectional scanning electron micrographs, while (c) and (d) are elemental maps of the same areas with (e and f) the corresponding energy dispersive X-ray spectroscopy line scans along the lines indicated in (a) and (b) by black arrows.

3.3 Frictional performance of the as-deposited coatings

The frictional performance of all samples was evaluated using reciprocating sliding experiments at room temperature (**Figure 3a**). For the bearing steel reference (REF), the coefficient of friction (COF) started at around 0.4 and quickly increased to 0.7 until levelling off at about 0.9. This can be considered a typical frictional behavior for steel-on-steel contact.

In contrast, the coated samples featured entirely different behaviors. The pure MXene coating did not show a beneficial effect for long under the chosen severe testing conditions since it only decreased friction for the first 200 s, after which it reached a high COF of 1.1. The high COF for the MXene coating is a result of coating removal and subsequent formation of debris, and oxides,

both acting as abrasives. We anticipate that the observed behavior can be related to the tribological testing conditions. Under an elevated contact pressure of 0.8 GPa, the MXene coating may be simply removed from the tribological contact zone, thus being deposited at the turning points of the wear track. The EDS analysis performed in the central region of the wear track did not detect the presence of Ti (zone 2 and 3 in **Figure S5**, Supporting Information). Additionally, the SEM micrographs confirm that the MXene coating was pushed away from the contact zone and accumulated on the edges of the wear scar (zone 1 in **Figure S5**, Supporting Information).

In contrast, an excellent friction reduction was observed for the MoS_2 coating (roughly four-fold reduction) in the first 600 s, in which it presented a COF of about 0.2, which aligns well with their calculated low interlayer adhesion. However, afterwards, the COF started to increase till the end of the experiment, thus reaching values of 0.4 and losing its beneficial lubrication effect.

The best frictional performance was observed for the hybrid coatings, which did not lose their lubrication effect during the entire test duration. Both hybrid coatings demonstrated a very stable and low COF until the end of the experiment. These results implied an almost six-fold COF reduction. No significant frictional differences were detectable between both hybrid coatings.

The experimental COFs before coating failure of some 2D materials (e.g. MXene $Ti_3C_2T_x$ [29,31,32,54], MoS_2 [55–57], graphene [58–61], h-BN [62,63], WS_2 [55,64]) have been summarized in **Table S5**, Supporting Information. Based on this table, it becomes evident that, although keeping the experimental testing conditions fairly similar, quite some experimental scattering related to the obtained COFs can be seen for the individual 2D materials. These differences may be connected to the quality and structure of the initial 2D materials, the coating fabrication method as well as the coatings' homogeneity, quality and adhesion, among others. Moreover, the observed scattering makes it challenging to directly compare the observed

experimental results with literature values. Therefore, we have experimentally evaluated not only the composite coatings, but also the pure 2D materials using the same equipment and testing conditions as well as the same batch of individual 2D materials.

Regarding the wear behavior, the overall coarse-scale appearance of the wear tracks was similar for both hybrids (**Figure 3c** and **d**). In contrast, non-uniform, patchy films were observed in the wear tracks of the MXene and MoS_2 coatings (**Figure S5** and **S6**, Supporting Information). Additionally, the wear track of the pure MXene and MoS_2 coatings were wider (width of about 600 and 300 µm, respectively) than those of the composites (~200 µm), which is also in accordance with the high COF of MXenes and the partial failure of MoS_2.

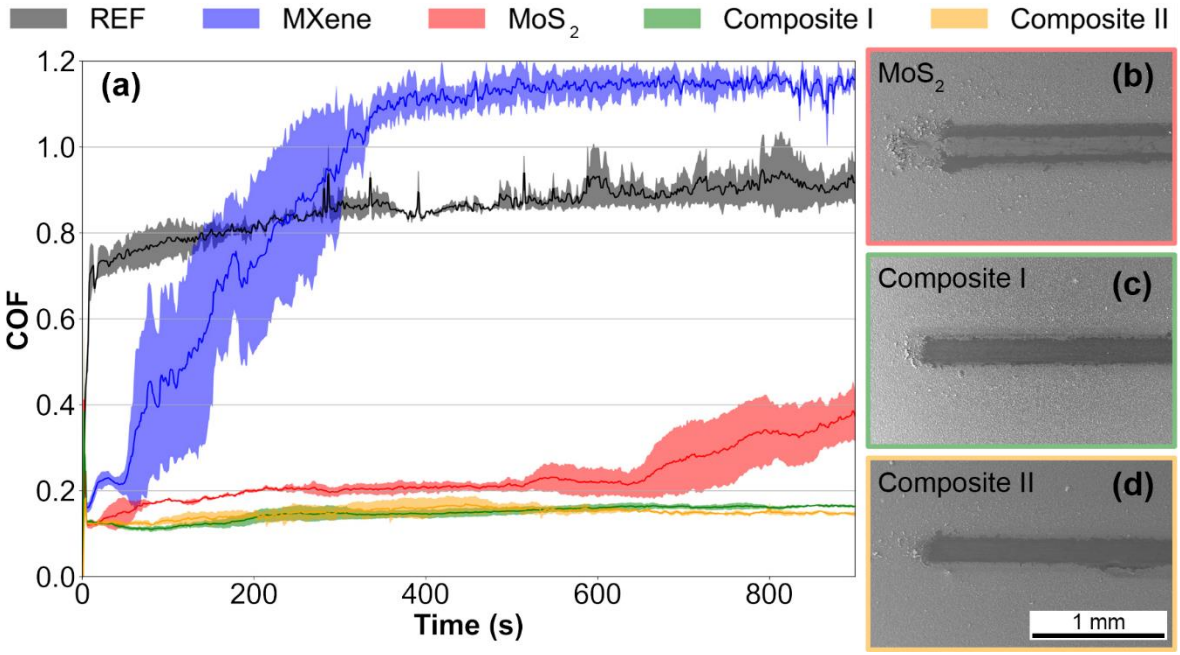

Figure 3. (a) Evolution of the COF of all samples. SEM micrographs of the wear tracks for (b) MoS_2, (c) Composite I and (d) Composite II. Mean values and the respective standard deviations of the three replicates are shown as plan line and shaded area, respectively.

3.4 Wear track analysis by XPS

To better understand the underlying mechanisms that govern the excellent frictional performance of the composites, the wear tracks were analyzed by XPS. Concerning the wear track of the pure MXene coating (**Figure S7a-d**), local XPS measurements confirmed that signal contributions from oxidized Ti are still visible within the wear track. This clearly indicates that MXenes have experienced oxidation under the tribo-mechanical impact thus transforming into TiO_2. Besides that, a mixture of F_3O_4, and α-Fe_2O_3 became evident when analyzing the Fe_{2p} peak, which connects with the removal of the MXene coating from the contact zone. Both observed aspects go hand in hand with the observed frictional evolution of the pure MXene coating shown in **Figure 3**. In contrast, the detected signal in the wear track of the pure MoS_2 coating confirmed only some slight oxidation, while a notable contribution that can be still assigned to the original MoS_2 signal (**Figure S7e-h**). However, there is a significant increase in the contribution of base sulfate species in the S_{2p} signal compared to the initial coating (**Figure S7e**), which can be associated with the formation of Mo-S-O groups [53]. The analysis of the Fe peak also demonstrates some substate exposure due to the presence of α-Fe_2O_3, while the $FeSO_4$ specie algins well with the increased sulfate signal. A summary of all fitted XPS data for the wear track of $Ti_3C_2T_x$ and MoS_2 coating after tribo-testing can be found in **Table S6** and **S7.**

Concerning Composite I (mixed composite coating), clear signals of Mo, Ti, and Fe are still present in the wear track (**Figure 4a-d**). In this context, a Ti peak located at around 459 eV can be seen, which can be attributed to TiO_2 thus confirming tribo-induced oxidation of the initial MXene coating. The analysis of the Mo_{3d} peak in the wear track confirms the existence of MoO_3 and original MoS_2. As seen in the peak fit of the Fe signal, the thermomechanical impact generates iron oxides and $FeSO_4$. Previous studies have also observed the formation of FeS_2 as a byproduct of tribo-chemical processes [48].

In contrast, the XPS data of the as-deposited Composite II did not exhibit any Ti signal (**Figure 4e-h**), which is consistent with the sequence order (MoS_2 being the topmost layer). The XPS analysis of the wear track detects a mixture of TiO_2 (originating from MXenes' tribo-oxidation), original MoS_2, and other oxidation products (MoO_3 and sulfate species), which is similar compared to the species observed for Composite I. The observed TiO_2 signal is indicative for the partial removal of the top-most MoS_2 layer, which aligns well with the cross-sectional TEM analysis. This implies that the substrate is still protected by a beneficial tribological layer, composed of the original coating materials and their tribo-induced oxidation products.

Comparing the relative contribution of the sulfate species of both composite coatings, an increase from 29 to 40 % becomes evident (detectable in the $Fe_{2p3/2}$ signal (**Figure 4h** as well as in **Table S8** and **S9**). This implies that Composite II contains more Mo- and Fe-based sulfates. It has been reported that these sulfates contribute to the generation of tribo-films and help to improve the respective wear resistance [48,65,66] (**Figure 3d**).

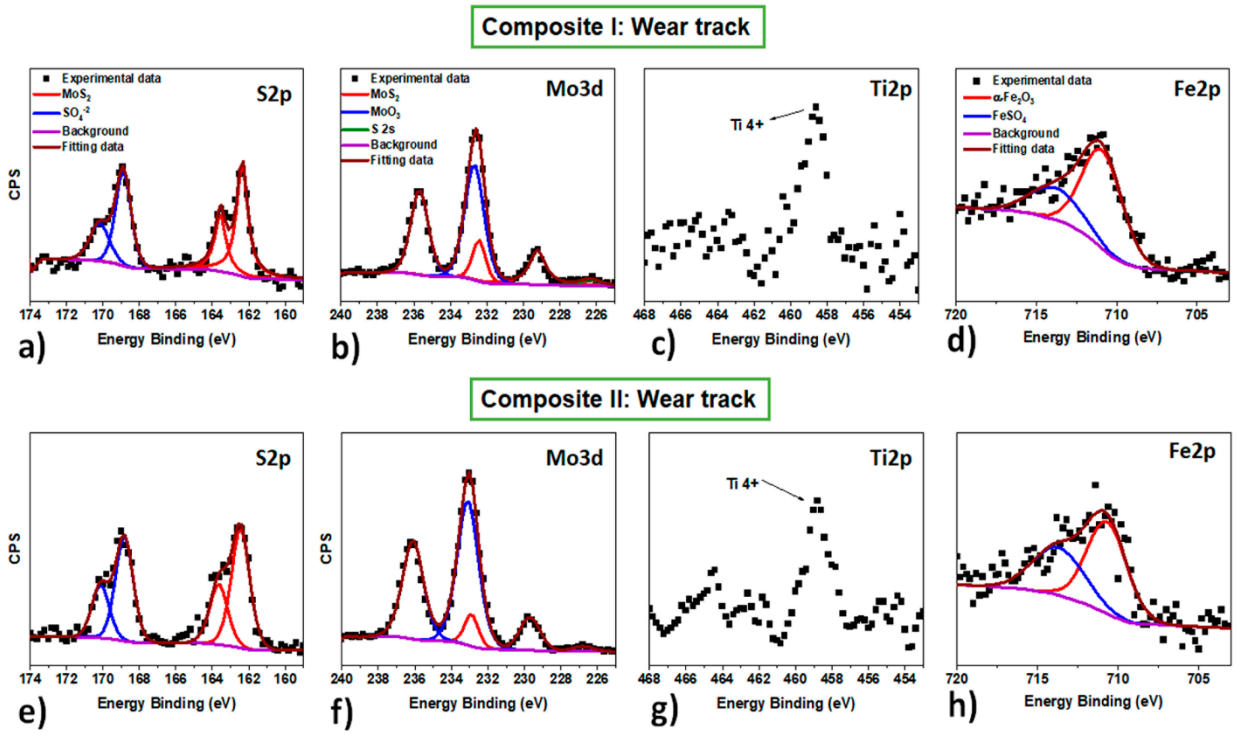

Figure 4. Detailed XPS analysis of the wear track for (a-d) Composite I and (e-h) Composite II coatings demonstrating the highly resolved, mathematically fitted peak regions of (a and e) S_{2p}, (b and f) Mo_{3d}, (c and g) Ti_{2p} and (d and h) Fe_{2p}, respectively. Each contribution assigned to a different chemical bond has been presented in a different color. Single dots resemble the experimental raw data, while the solid line represents the fitted spectrum.

Apart from the high-resolution XPS data, elemental XPS mapping **(Figure 5)** allowed for a detailed investigation of the superficial chemical states, which shed light on the chemical changes across the entire wear track.

In the case of the pure MXene coating, no Ti signal was detected in the wear track, while strong signals of Fe and O were observed. This implies the full removal of the initial MXene coating and the tribo-induced oxidation of the underlying substrate. This observation goes hand in hand with the measured evolution of the COF for this coating, which did not show any beneficial performance after a few minutes of testing. Concerning the wear track of the pure MoS_2 coating, some signals of S and Mo (carbide, attributable to as-deposited MoS_2) were detected in the outer perimeter of the wear track, while a more pronounced Mo signal (oxide) became evident in the center of the wear track. Additionally, strong Fe and O contributions are visible in the center of the wear track, which is again attributed to the removal of the MoS_2 coating, thus exposing the underlying substrate oxidized during tribological testing. This observation aligns well with the observed increase of the COF after a sliding time towards the end of the test (**Figure 3a**).

When comparing the elemental maps of the pure coatings with both hybrid coatings, notable differences can be observed. Regarding Composite I (mix of MXenes and MoS_2), contributions of S, Mo (carbide) and Ti were encountered in the wear track, which indicates the presence of a tribofilm containing MoS_2 and MXenes (in depth tribofilm analysis see section 3.4). These results corroborate the excellent frictional performance of Composite I (**Figure 3a**), showing the presence of MXenes and MoS_2 on the surface enduring the whole test. Moreover, signals of Mo (oxide), O,

and Fe indicated the contribution of oxidation in the wear track and the formation of a tribofilm. The excellent tribological performance of Composite I can be attributed to the lower W_{SEP} between MXene and MoS_2 layers as well as MoS_2 interfaces compared to pure MXene interfaces (**Figure 1**). Since a lower W_{SEP} implies more lubricity, the mixture of MXene and MoS_2 helps to reduce friction compared to the pure coatings. Additionally, the high adhesion of MoS_2 to iron and MXenes to iron oxide ensures that the lubricious film is not easily removed, thus extending the wear life.

With respect to Composite II (layer-by-layer coating having MoS_2 as top layer), the wear track still contains some S and Mo (carbide), which originate from the as-deposited MoS_2 top-layer. Besides that, a clear signal from Mo (oxide) can be seen inside the wear track, which points towards the oxidation of the outermost layers. Interestingly, the Ti signal is even stronger compared to the surrounding zones, which is due to the partial removal of the top MoS_2 layer and the exposure of the bottom MXene layer. The Fe signal was weaker for Composite II compared to the pure coatings, still indicating the presence of a thin coating after the tribological tests. These findings based on the XPS analyses imply that the top MoS_2 is only partially removed and oxidized. In this regard, sufficient lubricious MoS_2 and MXene are still available in the wear track, which induces a low COF as presented in **Figure 3**. The excellent tribological performance of Composite II can be explained again considering the calculated W_{SEP} in **Figure 1**. Due to the high interlayer adhesion between MXenes and the ferrous substrate, we assume that MXenes act as an intermediate anchoring layer between the substrate and MoS_2. This can help to avoid the complete exfoliation and removal of MoS_2 in Composite II. Therefore, we anticipate that the bottom MXene layer contributes towards the durability and longevity of the top MoS_2 layer by acting as an adhesion layer, thus improving additional coating-substrate interface adhesion.

Comparing the elemental maps in the wear tracks of both composites, higher concentrations of S, Mo, and Ti were encountered in Composite II, whereas a stronger Fe signal was detected in Composite I. This points towards a thicker and more homogenous tribofilm formed for Composite II, which might be due to the higher adhesion between MXene layers compared to MoS_2-MoS_2 or MoS_2-Ti_2CT_x, as well as their high adhesion to the ferrous oxides. Therefore, the bottom MXene layer in Composite II is more effective in increasing the adhesion of the coating to the substrate than the randomly distributed MXenes in Composite I.

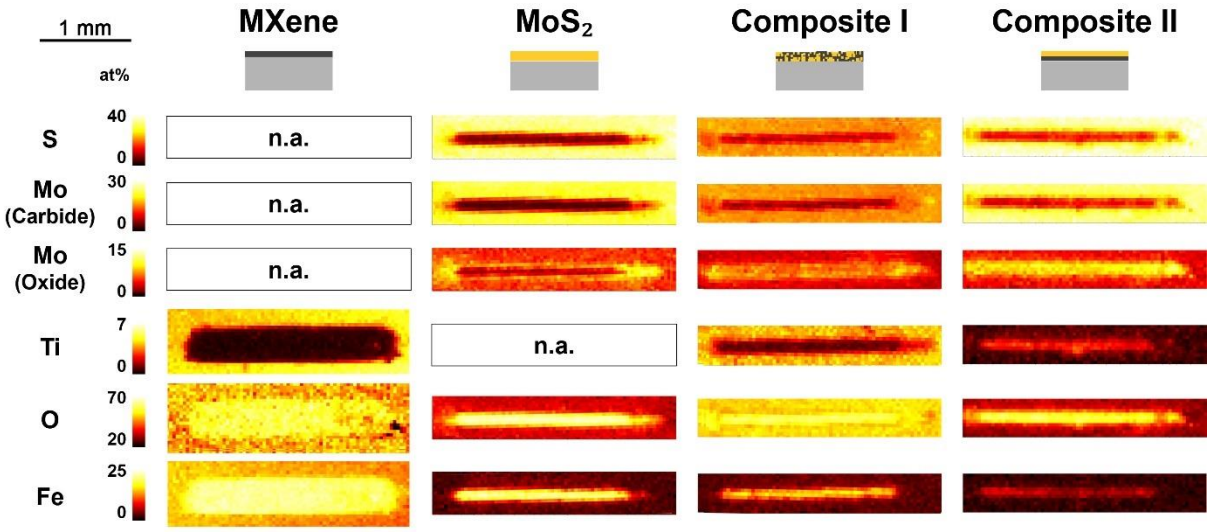

Figure 5. XPS element maps of the wear track for MXene, MoS_2, Composite I, and Composite II. The abbreviation *n.a.* stands for *not applicable*. Please note that brighter colors imply higher element concentrations, while different scales were adopted for every distinct element to improve data visibility and readability.

Moreover, elemental depth profiles in the middle of the wear tracks were measured by XPS for all coated samples to shed light on the distribution of the elements across the tribofilms (**Figure 6**). Related to the S distribution, it becomes evident that higher concentrations can be detected in surface regions. With increasing depth, the S signal decreases in an exponential fashion until almost disappearing at depths of about 200-300 nm (**Figure 6a**). For the MoS_2 coatings, the S

concentration was significantly lower compared to both hybrid coatings (roughly three-fold reduction). This result proves that the MoS_2 top layer of Composite II was still mainly intact after tribological testing, which agrees with the presented XPS surface mapping. Concerning the Mo distribution, the trend seen for the detected profiles of S stays unchanged (**Figure 6b**). The results of the S and Mo profiles are in accordance with the COF trend, being that MoS_2 samples presented higher friction than both hybrid coatings (**Figure 3a**). In fact, the higher S and Mo concentrations in the composites compared to MoS_2 indicate that the hybrid coatings were more prone to form stable tribofilms. MoS_2 samples lost their lubricious properties at the end of the tribological tests, whereas the composites performed low and stable friction for the entire test duration (**Figure 3a**).

Ti was only detected for hybrid samples and no traces were founded for the pure MXene coatings. This confirmed that the entire MXene layer was removed from the tribological contact zone without the possibility to form any beneficial tribolayer. This goes hand in hand with the discussed temporal evolution of the COF for the pure MXene coating, which shows an instantaneous increase reaching COF values above 1.1 (**Figure 6c**). For both hybrid coatings, the Ti signal was increased in surface-near regions, as observed for Mo and S, before decreasing in greater depths. In the case of Composite II, the maximum Ti concentration is shifted to a region further away from the surface (i.e., maximum is at a depth of roughly 100 nm) compared to Composite I, which aligns well with the as-deposited sandwich-like structure.

The Fe signal was divided into metallic and oxidic contributions to distinguish between substrate contributions (metallic signal) and tribo-oxidation (oxide signal) as well as to better estimate the tribofilm thickness after tribo-testing. In case of pure MXene coatings, the concentration of metallic Fe quickly increased with increasing depth, confirming the exposure of the metallic substrate and the removal of the as-deposited MXenes (**Figure 6d** and **e**). For MoS_2 and both the

metallic Fe signal monotonously increased with increasing depth reaching concentrations above 70 % for depths of about 200, 300, and 400 nm. This outcome corroborates well with the COF trend and element maps, showing again a superior tribological potential of the composites. Finally, the oxidic Fe signal was notably increased in superficial regions for the pure MXene and MoS_2 coatings, whereas significantly reduced contributions for Fe oxide were observed for both composite coatings. On the one hand, this clearly proves the ability of the hybrid coatings to form a beneficial tribofilm, thus protecting the substrate and preventing its oxidation and, on the other hand, the inefficiency of the pure coatings to form protecting tribofilms.

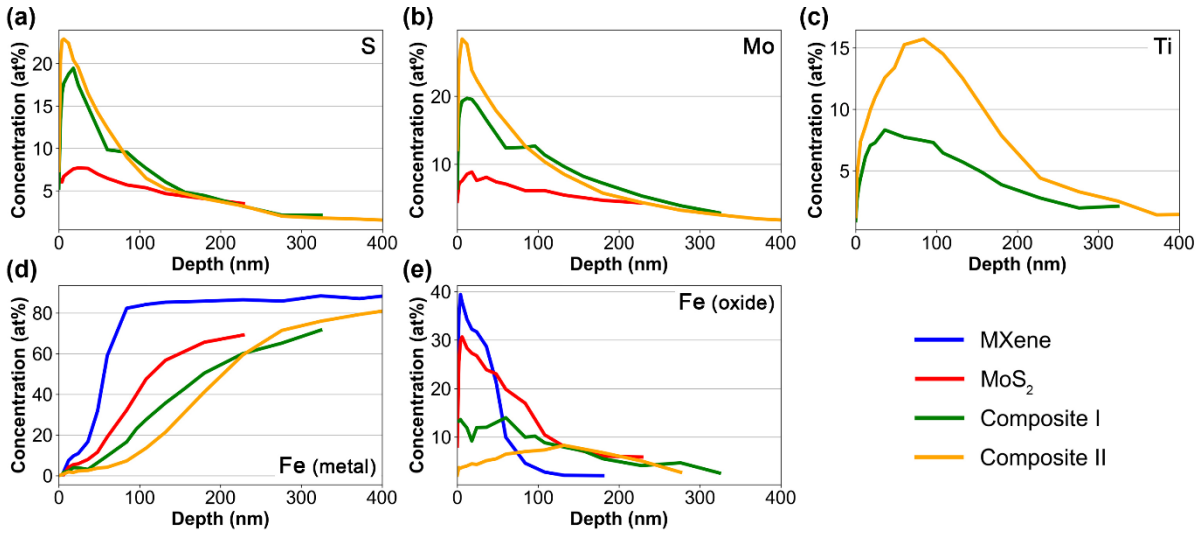

Figure 6. XPS elemental depth profile taken in the middle of the wear track for MXene, MoS_2, Composite I, and Composite II: (a) S, (b) Mo, (c) Ti, (d) Fe (metal) and (e) Fe (oxide).

3.4 Wear track analysis by TEM

To further characterize the structure of the formed tribofilms on the hybrid coatings, their wear tracks were analyzed by TEM. Several TEM specimens were prepared by FIB from the center and turning points of the wear tracks of Composite I and Composite II. Additional TEM specimens were prepared imaging the transition zone between initial coating and wear track (**Figure 7**).

The TEM analyses of the transition zones of both coatings demonstrate a reduction of the coating thickness as a result of tribological loading (**Figure 7a and b**). Nevertheless, the original coating morphology is retained with intermixed MXene and MoS_2 for Composite I and a sandwich-structure for Composite II (**Figure 7e-h**). In some positions, however, the coating becomes very thin or, for Composite II, the top MoS_2 layer is completely removed. This is accordance with the elemental mapping and depth profiles obtained by XPS demonstrating a much higher Ti concentration close to the surface for Composite II compared to Composite I. For Composite II, this implies that shear is mainly localized in the top MoS_2 layer, while the bottom MXene layer helps to increase the adhesion of the tribofilms to the substrate, thus contributing to the beneficial frictional performance and increased wear life. Additionally, oxygen diffusion into the substrate and the incorporation of iron and iron oxide particles into the tribofilm can be clearly observed (**Figure 7i-l**). These findings correlate well with the observed Fe signals in the XPS analyses.

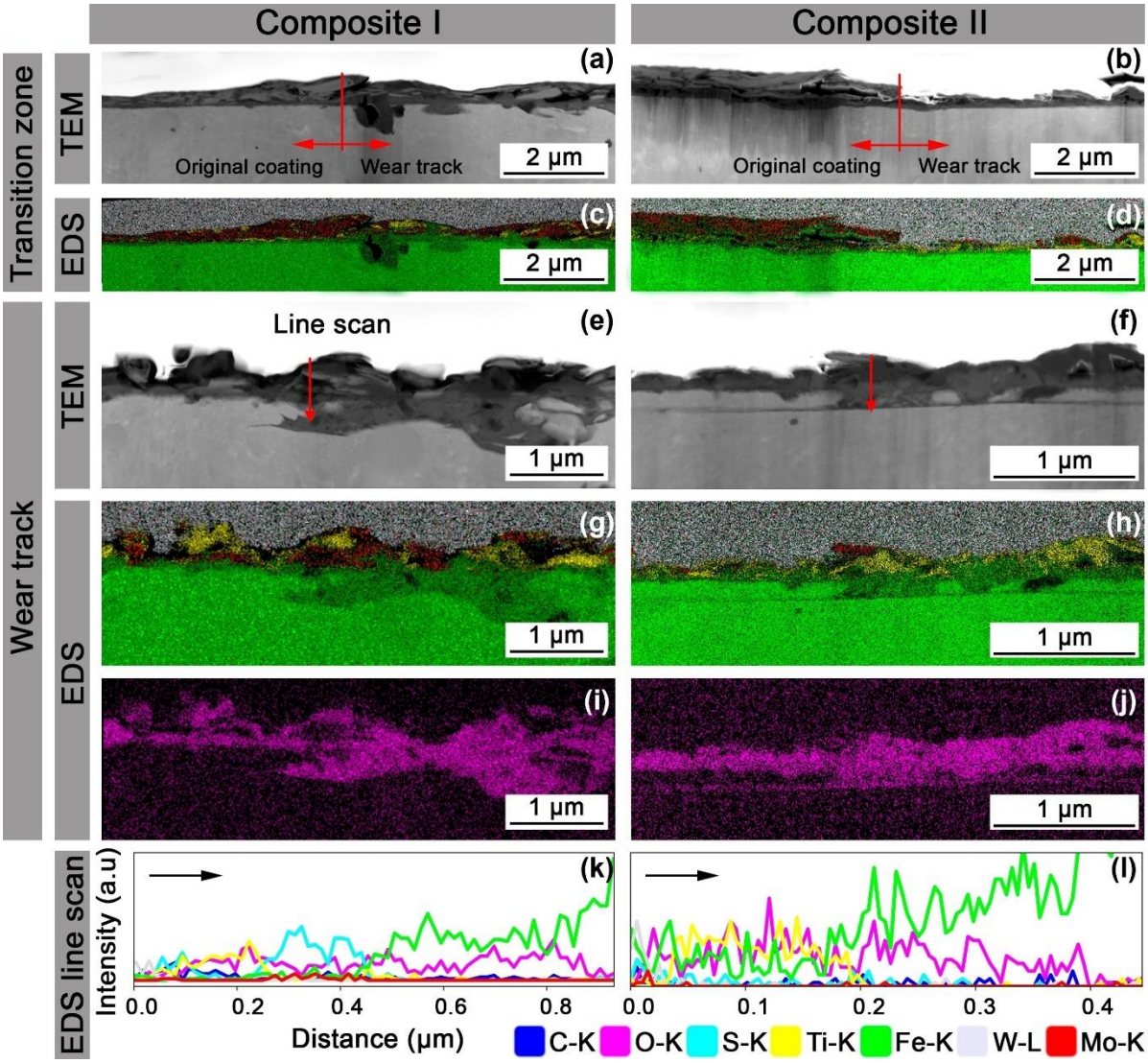

Figure 7. TEM analysis of the transition zone between original coating (left side of the images) and the wear track (images' right side) for (a) Composite I and (b) Composite II. (a) to (d) show the transition zone and corresponding elemental mappings, whereas (e) - (l) show images from the wear track and corresponding elemental mappings and EDS line scans along the lines indicated (e) and (f) with black arrows.

The exact positions for lamellae extraction inside the wear track (center and edge) are given in **Figures S8** and **S9** (Supporting Information). Particularly in the wear tracks' center positions, the formed tribofilms tend to be rather inhomogeneous with respect to their thickness (**Figure 8c** and **d**). Based on the SEM micrographs of the top surface, which were obtained to define the location of TEM specimen extraction, contrast differences (i.e., brighter and darker zones) can be noted.

The TEM analysis shows that these zones correlate with thinner or thicker tribofilms, respectively (**Figure 8c**,**d** and **i**,**j**). In accordance with the results demonstrated above for the wear tracks' transition zones, the tribofilms are partially completely removed or at least very thin (**Figure 8c - f**). In some cases, however, the initial coating structure with intermixed MoS_2/MXene (Composite I) or a defined layer structure (Composite II) is retained (**Figure 8i - l**). For Composite II, again the selective removal of the top MoS_2 layer in the thinner zones can be observed (**Figure 8c** and **d)**. The thicker portions of the tribofilms are analyzed in detail.

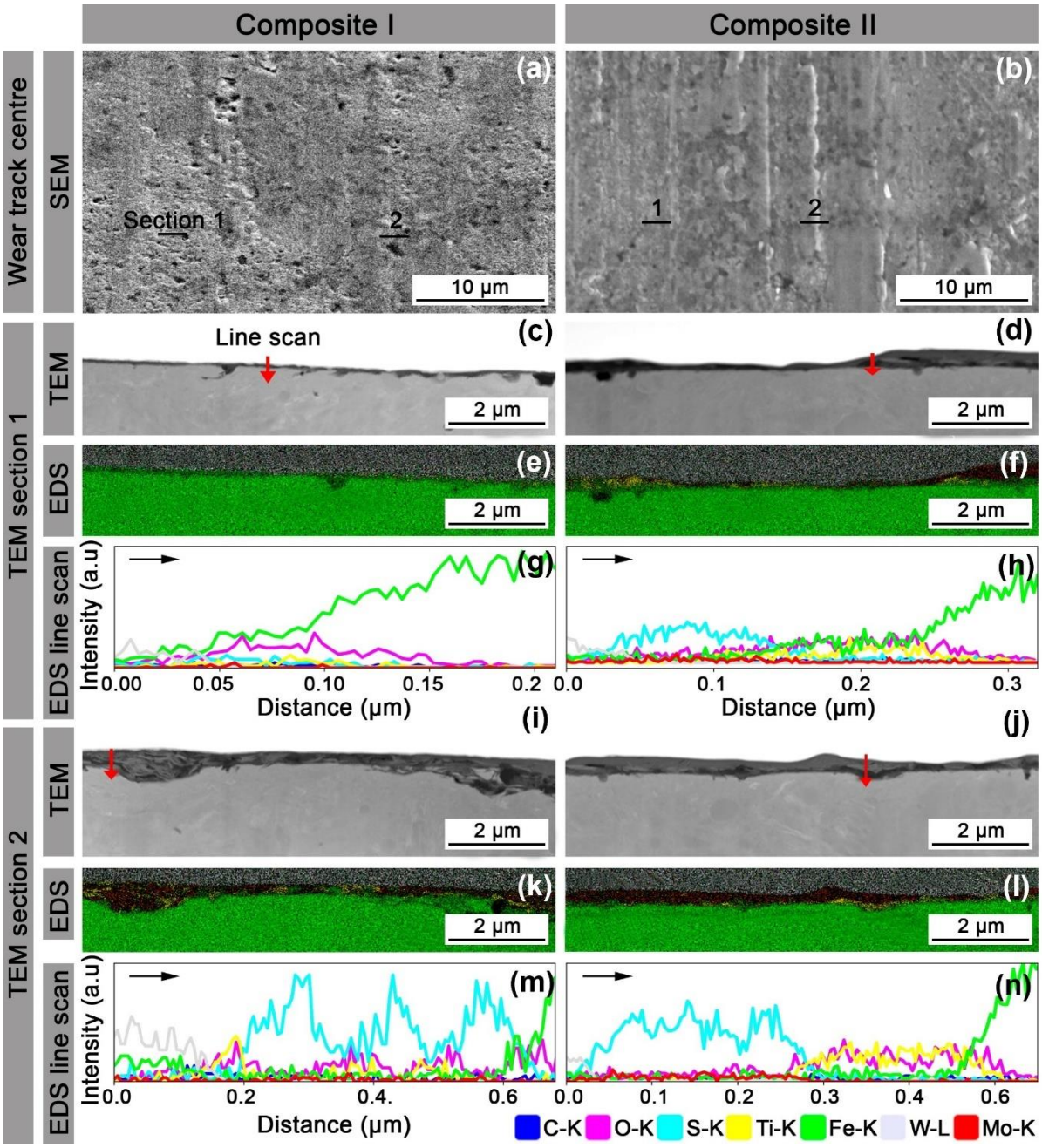

Figure 8. Analysis of the uniformity of the tribofilms formed in the center of the wear tracks on (a) Composite I and (b) Composite II. The (a) and (b) SEM images clearly demonstrate darker and brighter zones from where TEM specimens were extracted for further analysis. (c) - (n) TEM analysis below and the corresponding elemental mappings and EDS line scans along the lines indicated in (c), (d), (i), and (j) with black arrows demonstrate the inhomogeneity of the wear tracks.

Figure 9 shows the TEM analysis of the wear track's center position for Composite I. HR-TEM provides information on the structure of the tribofilms, while selected area electron diffraction (SAED) and elemental mappings by TEM-EDS of specific areas allow for an analysis of the tribofilm's crystallinity and chemical composition. After tribological testing, the thickness of the tribofilm on Composite I is inhomogeneous ranging from roughly 220 nm to > 820 nm (**Figure 9a**). Closer investigation of the tribofilm by HR-TEM clearly demonstrates a tribofilm consisting of amorphous and layered structures (**Figure 9b-d**). SAED confirms the presence of crystalline (well defined larger diffraction spots), nanocrystalline (smaller spots, partially forming well defined diffraction rings according to their crystal phases), and amorphous phases (diffuse diffraction rings) inside the tribofilm (**Figure 9e** and **Figure S10**, Supporting Information). The amorphous phases are mainly found close to the tribological interface as these are the positions with the highest pressure and temperature leading to thermo-mechanical amorphization. Close to the substrate surface, SAED verifies nanocrystalline Fe_2O_3, while inside the tribofilm a mixture of MoS_2 and Ti_3C_2 prevails (P63/mmc space group). The chemical composition of the tribofilm is further analyzed by elemental mapping (**Figure 9f**). The structure of the tribofilm after tribo-testing still resembles the initial coating structure, for which Ti-rich phases are randomly intermixed with Mo- and S-rich phases. Additionally, a significant amount of oxygen can be found inside the tribofilm. Taking these points into consideration, we anticipate that the MXene/MoS_2 hybrid coating is partially amorphized or converted into nanocrystals as a result of mechanical shearing under the high acting contact pressures (globally 0.8 GPa, higher peak loads are expected). Additionally, the MXene and MoS_2 nano-sheets are partially oxidized due to tribochemical reactions. Nevertheless, there are still many intact 2D nano-sheets as well as MXene/MoS_2 interfaces in the tribofilm (**Figure 9**c), which can provide low shear strength

(**Figure 1**), resulting in the low friction observed in **Figure 3a**. Similar observations can be made at the edge of the wear track (**Figure S11**, Supporting Information), where the tribofilm is generally thinner.

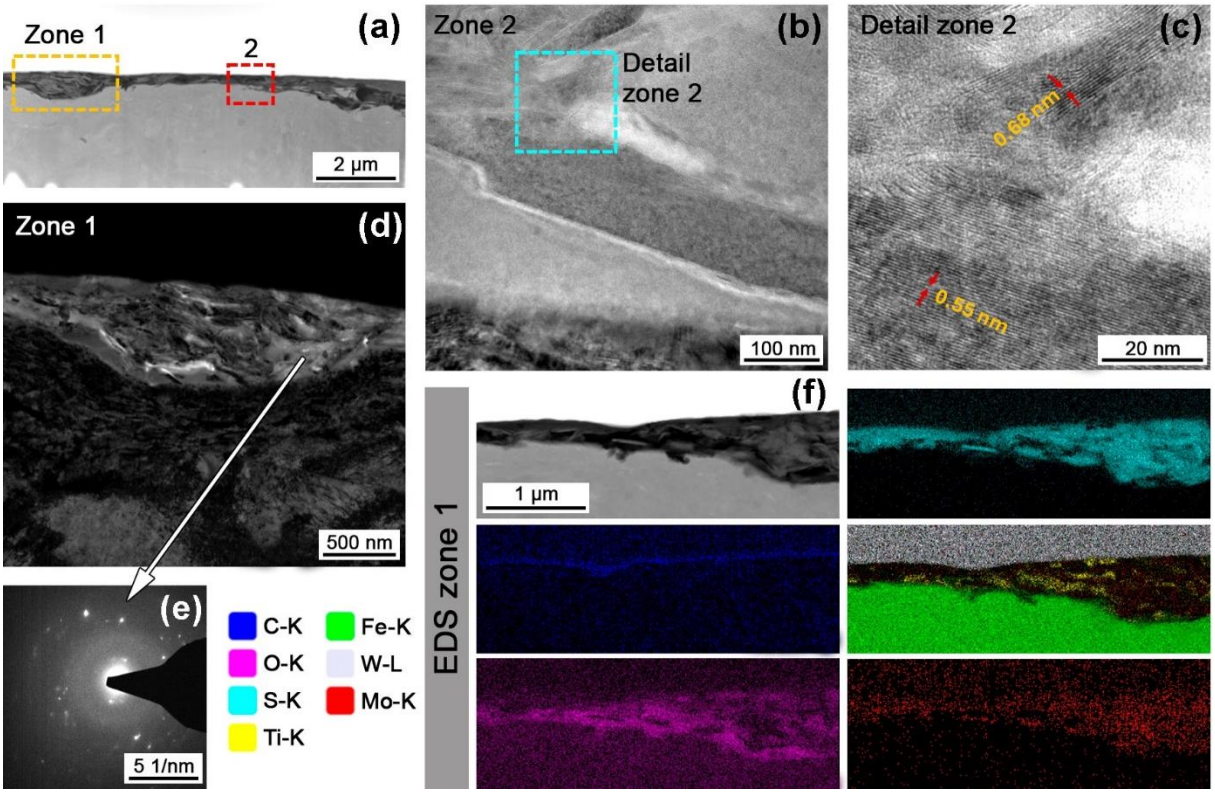

Figure 9. TEM analysis of the wear track on Composite I. (a) – (d) TEM images with different magnifications provide information on the structure of the tribofilm, and (e) selected area electron diffraction patterns and (f) elemental mappings demonstrate the phase and the chemical composition of the tribofilm.

Figure 10 shows the corresponding TEM analysis of the wear track's center position for Composite II. Similar to Composite I, HR-TEM clearly indicates a mixture of amorphous, crystalline, and nanocrystalline phases inside the tribofilm, where layered nano-sheets can be easily distinguished (**Figure 10a-c**). The presence of amorphous phases and crystalline MoS_2 and $Ti_3C_2T_x$ is confirmed by SAED (**Figure 10 d-f** and **Figure S12**, Supporting Information). Stronger

amorphization has been observed for the zones close to the tribological interface (**Figure S12**, Supporting Information). As verified by the elemental mapping, the structure of the tribofilm strongly resembles the initial coating with a Mo-rich top-layer and a Ti-rich layer below, thus maintaining the original sandwich-like structure (**Figure 10 g**). These observations hold also true for the edge of the wear track, where the layered structure with Mo-rich phases on top and Ti-rich phases below is retained (**Figure S13**, Supporting Information). Nevertheless, there are still sufficient crystalline 2D structures in the tribofilm to provide low shear and to efficiently reduce friction.

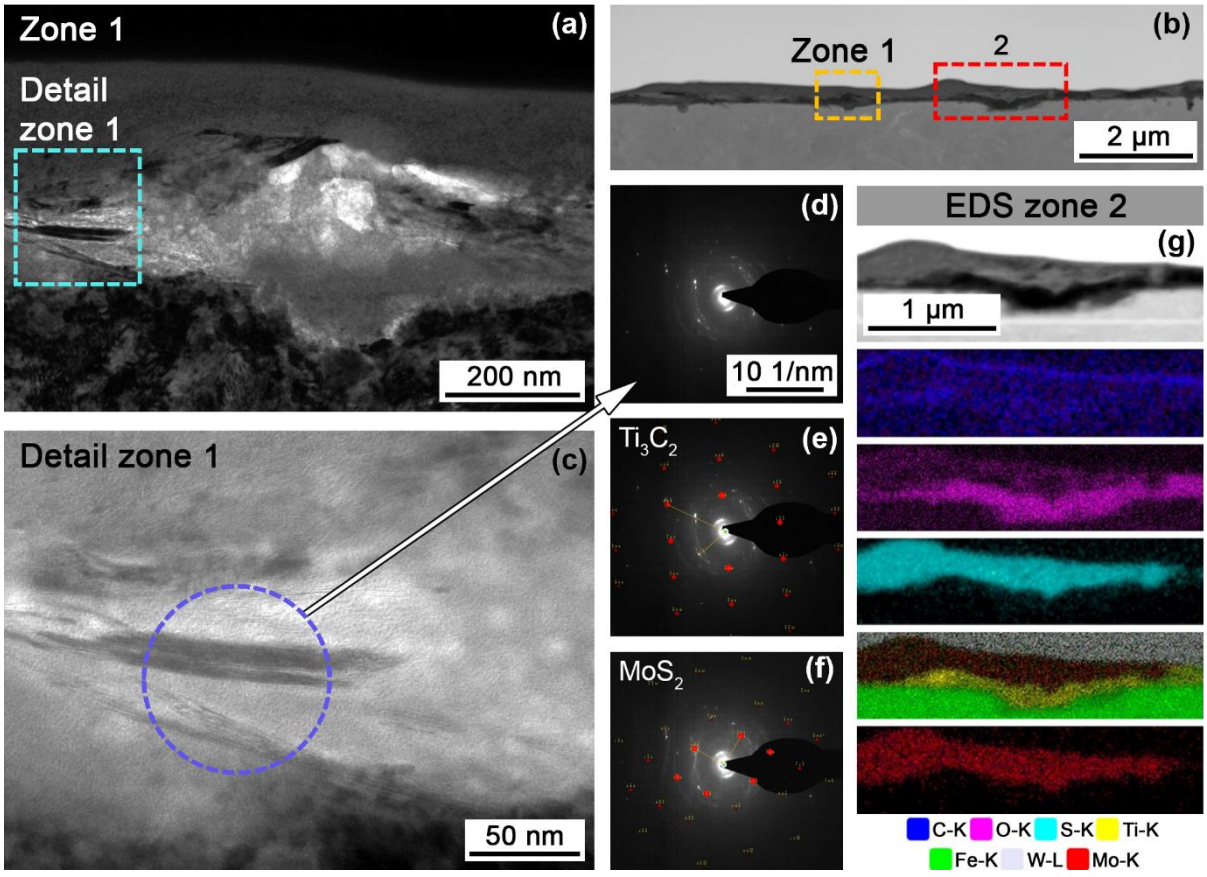

Figure 10. TEM analysis of the wear track on Composite II. (a) – (c) TEM images with different magnifications provide information on the structure of the tribofilm, and (d) – (f) selected area electron diffraction patterns and (g) elemental mappings demonstrate the phase and the chemical composition of the tribofilm on Composite II.

Considering the numerical calculations as well as XPS and TEM results for both composites, it becomes evident that the coatings' structure remained mainly intact after tribological testing with little intermixing of the constituents. For Composite I, the low W_{SEP} for mixed MXene/MoS_2 interfaces, which is similar to MoS_2-MoS_2 interfaces, is the major factor responsible for the improved lubricious properties. Since MoS_2 tends to adhere to pure iron and MXenes demonstrated an improved adhesion to iron oxide, the formed tribofilm can stick to the substrate independent of the respective chemical state of the substrate. This helps to extend the useful lifetime of low friction tribofilms. In the case of Composite II, the stronger adhesion of MXenes to iron oxide acts as an adhesion layer, while the resulting frictional performance is mainly governed by the low interlayer adhesion of adjacent MoS_2 layers.

4. CONCLUSIONS

The tribological performance of multi-layer $Ti_3C_2T_x$, MoS_2, and two $Ti_3C_2T_x$ /MoS_2 hybrid coatings have been experimentally scrutinized under dry reciprocating sliding tests. Results were corroborated via numerical simulations of the adhesion forces between the layers and to different substrates. The friction and wear performance as well as tribolayer formation were holistically analyzed with a complementary characterization approach including SEM-EDS, FIB, XPS and TEM. Based on the acquired results, the following conclusions can be drawn:

- Pure MXene coatings did not bring any tribological beneficial effect under the respective testing conditions compared to the steel reference (REF), whereas pure MoS_2 coatings presented approximately a four-fold friction reduction. Both MXene/MoS_2 hybrid coatings (random mixture and sandwich-like) significantly reduced friction (roughly six-fold

reduction compared to REF) even when compared to the pure coating materials. Low and steady COF values of around 0.15 were maintained for the entire test duration due to the formation of a stable tribofilm.

- No significant wear protection was observed for the pure $Ti_3C_2T_x$ coating (coating removal), whereas the pure MoS_2 considerably reduced wear, although partially losing its lubricity towards the end of the test duration. The hybrid MXene/MoS_2 coatings presented a superior wear behavior, displaying the highest wear resistance.
- Numerical calculations validated the experimental results, being that MXene/MoS_2 hybrids demonstrate an excellent frictional performance with low interlayer friction and high adhesion to ferrous substrates, outperforming the pure MXene and MoS_2 coatings.
- The coating structure of both composites remained intact even after the tribological tests, showing the synergic effect between $Ti_3C_2T_x$ and MoS_2. Particularly, the layer-by-layer structure still presented a MoS_2 top-layer after tribo-testing. The adhesion force between $Ti_3C_2T_x$ and MoS_2 seemed to be the governing mechanisms to enhance the formation of the stable tribofilm.
- Consequently, hybrid MXene/MoS_2 coatings present a tremendous potential to be used as solid lubricant for severe tribological application (0.8 GPa), presenting both low friction and superior wear resistance.

Author Contributions

Guido Boidi: Conceptualization, Formal analysis, Investigation, Data Curation, Writing - Original Draft, Visualization, Project administration **Dario Zambrano:** Formal analysis, Investigation, Data Curation, Visualization, Methodology **Sabine Schwarz:** Methodology,

Writing – Review & Editing, Visualization **Edoardo Marquis:** Numerical Simulation, Formal Analysis, Data Curation, Writing - Review & Editing **Markus Varga:** Resources, Writing - Review & Editing, Visualization, Funding acquisition **Manel Rodríguez Ripoll:** Writing - Review & Editing **Ewald Badisch:** Writing - Review & Editing, Funding acquisition **Maria Clelia Righi:** Resources, Writing - Review & Editing, Supervision **Carsten Gachot:** Resources, Writing - Review & Editing, Supervision **Philipp G. Grützmacher:** Formal analysis, Data Curation, Writing - Original Draft, Visualization **Andreas Rosenkranz:** Conceptualization, Resources, Writing - Original Draft, Supervision, Project administration

Funding Sources

Austrian COMET-Programme (Project InTribology1, no. 872176), Fondecyt Regular 1220331, Fondequip EQM190057, ERC SLIDE 865633

Notes

Authors approve ethics in publishing and consent to participate thereof.

The authors declare consent for publication.

The authors declare no competing interests.

ACKNOWLEDGMENTS

This work was funded by the "Austrian COMET-Programme" (Project InTribology1, no. 872176) under the scope of K2 InTribology and was developed in collaboration with the "Excellence Centre of Tribology" (AC2T research GmbH). A. Rosenkranz gratefully acknowledges the financial support given by ANID within the project Fondecyt Regular 1220331 and Fondequip EQM190057. These results are part of the "Advancing Solid Interface and

Lubricants by First Principles Material Design (SLIDE)" project that has received funding from the European Research Council (ERC) under the European Union's Horizon 2020 research and innovation program (Grant agreement No. 865633).

REFERENCES

[1] M. Woydt, Material efficiency through wear protection – The contribution of tribology for reducing CO2 emissions, Wear. 488–489 (2022) 204134. https://doi.org/10.1016/j.wear.2021.204134.

[2] K. Holmberg, A. Erdemir, The impact of tribology on energy use and CO2 emission globally and in combustion engine and electric cars, Tribol. Int. 135 (2019) 389–396. https://doi.org/10.1016/j.triboint.2019.03.024.

[3] M. Marian, D. Berman, A. Rota, R.L. Jackson, A. Rosenkranz, Layered 2D Nanomaterials to Tailor Friction and Wear in Machine Elements—A Review, Adv. Mater. Interfaces. 9 (2022) 2101622. https://doi.org/10.1002/admi.202101622.

[4] B.R. Manu, A. Gupta, A.H. Jayatissa, Tribological Properties of 2D Materials and Composites—A Review of Recent Advances, Materials (Basel). 14 (2021) 1630. https://doi.org/10.3390/ma14071630.

[5] J.H. Lee, D.-H. Cho, B.H. Park, J.S. Choi, Nanotribology of 2D materials and their macroscopic applications, J. Phys. D. Appl. Phys. 53 (2020) 393001. https://doi.org/10.1088/1361-6463/ab9670.

[6] K.S. Novoselov, A.K. Geim, S. V. Morozov, D. Jiang, Y. Zhang, S. V. Dubonos, I. V. Grigorieva, A.A. Firsov, Electric Field Effect in Atomically Thin Carbon Films, Science (80-.). 306 (2004) 666–669. https://doi.org/10.1126/science.1102896.

[7] D. Akinwande, C.J. Brennan, J.S. Bunch, P. Egberts, J.R. Felts, H. Gao, R. Huang, J.-S. Kim, T. Li, Y. Li, K.M. Liechti, N. Lu, H.S. Park, E.J. Reed, P. Wang, B.I. Yakobson, T. Zhang, Y.-W. Zhang, Y. Zhou, Y. Zhu, A review on mechanics and mechanical properties of 2D materials—Graphene and beyond, Extrem. Mech. Lett. 13 (2017) 42–77. https://doi.org/10.1016/j.eml.2017.01.008.

[8] G.G. Naumis, S. Barraza-Lopez, M. Oliva-Leyva, H. Terrones, Electronic and optical properties of strained graphene and other strained 2D materials: a review, Reports Prog. Phys. 80 (2017) 096501. https://doi.org/10.1088/1361-6633/aa74ef.

[9] H. Xiao, S. Liu, 2D nanomaterials as lubricant additive: A review, Mater. Des. 135 (2017) 319–332. https://doi.org/10.1016/j.matdes.2017.09.029.

[10] T.W. Scharf, S. V. Prasad, Solid lubricants: a review, J. Mater. Sci. 48 (2013) 511–531. https://doi.org/10.1007/s10853-012-7038-2.

[11] J. Zhao, Y. Huang, Y. He, Y. Shi, Nanolubricant additives: A review, Friction. 9 (2021) 891–917. https://doi.org/10.1007/s40544-020-0450-8.

[12] I. Minami, Molecular Science of Lubricant Additives, Appl. Sci. 7 (2017) 445. https://doi.org/10.3390/app7050445.

[13] Q. Gao, S. Liu, K. Hou, Z. Li, J. Wang, Graphene-Based Nanomaterials as Lubricant Additives: A Review, Lubricants. 10 (2022) 273. https://doi.org/10.3390/lubricants10100273.

[14] M. Naguib, M. Kurtoglu, V. Presser, J. Lu, J. Niu, M. Heon, L. Hultman, Y. Gogotsi, M.W. Barsoum, Two-Dimensional Nanocrystals Produced by Exfoliation of Ti3AlC2, Adv. Mater. 23 (2011) 4248–4253. https://doi.org/10.1002/adma.201102306.

[15] M. Dadashi Firouzjaei, M. Karimiziarani, H. Moradkhani, M. Elliott, B. Anasori, MXenes:

The two-dimensional influencers, Mater. Today Adv. 13 (2022) 100202. https://doi.org/10.1016/j.mtadv.2021.100202.

[16] Y. Gogotsi, B. Anasori, The Rise of MXenes, ACS Nano. 13 (2019) 8491–8494. https://doi.org/10.1021/acsnano.9b06394.

[17] A. Rosenkranz, M.C. Righi, A. V. Sumant, B. Anasori, V.N. Mochalin, Perspectives of 2D MXene Tribology, Adv. Mater. (2022) 2207757. https://doi.org/10.1002/adma.202207757.

[18] Y. Wang, T. Guo, Z. Tian, K. Bibi, Y. Zhang, H.N. Alshareef, MXenes for Energy Harvesting, Adv. Mater. 34 (2022) 2108560. https://doi.org/10.1002/adma.202108560.

[19] D. Xiong, Y. Shi, H.Y. Yang, Rational design of MXene-based films for energy storage: Progress, prospects, Mater. Today. 46 (2021) 183–211. https://doi.org/https://doi.org/10.1016/j.mattod.2020.12.004.

[20] Y. Tian, Y. An, B. Xu, MXene-based materials for advanced nanogenerators, Nano Energy. 101 (2022) 107556. https://doi.org/https://doi.org/10.1016/j.nanoen.2022.107556.

[21] B.C. Wyatt, A. Rosenkranz, B. Anasori, 2D MXenes: Tunable Mechanical and Tribological Properties, Adv. Mater. 33 (2021) 2007973. https://doi.org/10.1002/adma.202007973.

[22] A. Rosenkranz, Y. Liu, L. Yang, L. Chen, 2D nano-materials beyond graphene: from synthesis to tribological studies, Appl. Nanosci. 10 (2020) 3353–3388. https://doi.org/10.1007/s13204-020-01466-z.

[23] G. Boidi, J.C. F. de Queiróz, F.J. Profito, A. Rosenkranz, Ti3C2Tx MXene Nanosheets as Lubricant Additives to Lower Friction under High Loads, Sliding Ratios, and Elevated Temperatures, ACS Appl. Nano Mater. 6 (2023) 729–737. https://doi.org/10.1021/acsanm.2c05033.

[24] P.G. Grützmacher, R. Neuhauser, K. Stagel, K. Bica-Schröder, G. Boidi, C. Gachot, A.

Rosenkranz, Combining Tailored Ionic Liquids with Ti 3 C 2 T x MXenes for an Enhanced Load-Carrying Capacity Under Boundary Lubrication, Adv. Eng. Mater. (2023). https://doi.org/10.1002/adem.202300721.

[25] M. Marian, S. Tremmel, S. Wartzack, G. Song, B. Wang, J. Yu, A. Rosenkranz, Mxene nanosheets as an emerging solid lubricant for machine elements – Towards increased energy efficiency and service life, Appl. Surf. Sci. 523 (2020) 146503. https://doi.org/10.1016/j.apsusc.2020.146503.

[26] J.Y.A. Hurtado, P.G. Grützmacher, J.M. Henríquez, D. Zambrano, B. Wang, A. Rosenkranz, Solid Lubrication Performance of Few- and Multilayer Ti3C2Tx Coatings, Adv. Eng. Mater. 24 (2022) 2200755. https://doi.org/10.1002/adem.202200755.

[27] H. Zhang, L. Wang, A. Zhou, C. Shen, Y. Dai, F. Liu, J. Chen, P. Li, Q. Hu, Effects of 2-D transition metal carbide Ti 2 CT x on properties of epoxy composites, RSC Adv. 6 (2016) 87341–87352. https://doi.org/10.1039/C6RA14560D.

[28] H. Yan, M. Cai, W. Li, X. Fan, M. Zhu, Amino-functionalized Ti3C2T with anti-corrosive/wear function for waterborne epoxy coating, J. Mater. Sci. Technol. 54 (2020) 144–159. https://doi.org/10.1016/j.jmst.2020.05.002.

[29] P.G. Grützmacher, S. Suarez, A. Tolosa, C. Gachot, G. Song, B. Wang, V. Presser, F. Mücklich, B. Anasori, A. Rosenkranz, Superior Wear-Resistance of Ti3C2Tx Multilayer Coatings, ACS Nano. 15 (2021) 8216–8224. https://doi.org/10.1021/acsnano.1c01555.

[30] M. Marian, G.C. Song, B. Wang, V.M. Fuenzalida, S. Krauß, B. Merle, S. Tremmel, S. Wartzack, J. Yu, A. Rosenkranz, Effective usage of 2D MXene nanosheets as solid lubricant – Influence of contact pressure and relative humidity, Appl. Surf. Sci. 531 (2020) 147311. https://doi.org/10.1016/j.apsusc.2020.147311.

[31] A. Rosenkranz, P.G. Grützmacher, R. Espinoza, V.M. Fuenzalida, E. Blanco, N. Escalona, F.J. Gracia, R. Villarroel, L. Guo, R. Kang, F. Mücklich, S. Suarez, Z. Zhang, Multi-layer Ti3C2Tx-nanoparticles (MXenes) as solid lubricants – Role of surface terminations and intercalated water, Appl. Surf. Sci. 494 (2019) 13–21. https://doi.org/10.1016/j.apsusc.2019.07.171.

[32] W. Lian, Y. Mai, C. Liu, L. Zhang, S. Li, X. Jie, Two-dimensional Ti3C2 coating as an emerging protective solid-lubricant for tribology, Ceram. Int. 44 (2018) 20154–20162. https://doi.org/10.1016/j.ceramint.2018.07.309.

[33] S. Zhang, T. Ma, A. Erdemir, Q. Li, Tribology of two-dimensional materials: From mechanisms to modulating strategies, Mater. Today. 26 (2019) 67–86. https://doi.org/10.1016/j.mattod.2018.12.002.

[34] S. Luo, T. Alkhidir, S. Mohamed, S. Anwer, B. Li, J. Fu, K. Liao, V. Chan, Investigation of interfacial interaction of graphene oxide and Ti3C2Tx (MXene) via atomic force microscopy, Appl. Surf. Sci. 609 (2023) 155303. https://doi.org/10.1016/j.apsusc.2022.155303.

[35] Y. Li, S. Huang, C. Wei, D. Zhou, B. Li, C. Wu, V.N. Mochalin, Adhesion Between MXenes and Other 2D Materials, ACS Appl. Mater. Interfaces. 13 (2021) 4682–4691. https://doi.org/10.1021/acsami.0c18624.

[36] E. Marquis, M. Cutini, B. Anasori, A. Rosenkranz, M.C. Righi, Nanoscale MXene Interlayer and Substrate Adhesion for Lubrication: A Density Functional Theory Study, ACS Appl. Nano Mater. 5 (2022) 10516–10527. https://doi.org/10.1021/acsanm.2c01847.

[37] X. Yin, J. Jin, X. Chen, A. Rosenkranz, J. Luo, Ultra-Wear-Resistant MXene-Based Composite Coating via in Situ Formed Nanostructured Tribofilm, ACS Appl. Mater.

Interfaces. 11 (2019) 32569–32576. https://doi.org/10.1021/acsami.9b11449.

[38] S. Huang, K.C. Mutyala, A.V. Sumant, V.N. Mochalin, Achieving superlubricity with 2D transition metal carbides (MXenes) and MXene/graphene coatings, Mater. Today Adv. 9 (2021) 100133. https://doi.org/10.1016/j.mtadv.2021.100133.

[39] A. Macknojia, A. Ayyagari, D. Zambrano, A. Rosenkranz, E. V. Shevchenko, D. Berman, Macroscale Superlubricity Induced by MXene/MoS 2 Nanocomposites on Rough Steel Surfaces under High Contact Stresses, ACS Nano. 17 (2023) 2421–2430. https://doi.org/10.1021/acsnano.2c09640.

[40] G. Boidi, D. Zambrano, M.I. Broens, D. Moncada, M. Varga, M.R. Ripoll, E. Badisch, N. Escalona, P.G. Grützmacher, C. Gachot, A. Rosenkranz, Influence of ex-situ annealing on the friction and wear performance of multi-layer Ti3C2T coatings, Appl. Mater. Today. 36 (2024) 102020. https://doi.org/10.1016/j.apmt.2023.102020.

[41] A. Rosenkranz, B. Wang, D. Zambrano, J. Marqués Henríquez, J.Y. Aguilar-Hurtado, E. Marquis, P. Restuccia, B.C. Wyatt, M.C. Righi, B. Anasori, Solid-lubrication performance of Ti3C2T - Effect of tribo-chemistry and exfoliation, Mater. Today Nano. 25 (2024) 100464. https://doi.org/10.1016/j.mtnano.2024.100464.

[42] E. Marquis, F. Benini, B. Anasori, A. Rosenkranz, M.C. Righi, Effect of vacancies and edges in promoting water chemisorption on titanium-based MXenes, Nano Converg. 10 (2023) 16. https://doi.org/10.1186/s40580-023-00364-8.

[43] V. Natu, M.W. Barsoum, MXene Surface Terminations: A Perspective, J. Phys. Chem. C. 127 (2023) 20197–20206. https://doi.org/10.1021/acs.jpcc.3c04324.

[44] T. Stirner, D. Scholz, J. Sun, Convergence of surface energy calculations for various methods: (0 0 1), (0 1 2), (1 0 0) hematite and the applicability of the standard approach, J.

Phys. Condens. Matter. 32 (2020) 185002. https://doi.org/10.1088/1361-648X/ab6f88.

[45] M. Wolloch, G. Losi, M. Ferrario, M.C. Righi, High-throughput screening of the static friction and ideal cleavage strength of solid interfaces, Sci. Rep. 9 (2019) 17062. https://doi.org/10.1038/s41598-019-49907-2.

[46] V. Natu, M. Benchakar, C. Canaff, A. Habrioux, S. Célérier, M.W. Barsoum, A critical analysis of the X-ray photoelectron spectra of Ti3C2Tz MXenes, Matter. 4 (2021) 1224–1251. https://doi.org/10.1016/j.matt.2021.01.015.

[47] J. Halim, K.M. Cook, M. Naguib, P. Eklund, Y. Gogotsi, J. Rosen, M.W. Barsoum, X-ray photoelectron spectroscopy of select multi-layered transition metal carbides (MXenes), Appl. Surf. Sci. 362 (2016) 406–417. https://doi.org/10.1016/j.apsusc.2015.11.089.

[48] D.F. Zambrano-Mera, M.I. Broens, R. Villarroel, R. Espinoza-Gonzalez, J.Y. Aguilar-Hurtado, B. Wang, S. Suarez, F. Mücklich, P. Valenzuela, W. Gacitúa, A. Rosenkranz, Solid Lubrication Performance of Sandwich Ti3C2Tx-MoS2 Composite Coatings, Appl. Surf. Sci. (2023) 158295. https://doi.org/10.1016/j.apsusc.2023.158295.

[49] J.F. Moulder, J. Chastain, Handbook of X-ray Photoelectron Spectroscopy: A Reference Book of Standard Spectra for Identification and Interpretation of XPS Data, Physical Electronics Division, Perkin-Elmer Corporation, 1992. https://books.google.at/books?id=A_XGQgAACAAJ.

[50] D. Ganta, S. Sinha, R.T. Haasch, 2-D Material Molybdenum Disulfide Analyzed by XPS, Surf. Sci. Spectra. 21 (2014) 19–27. https://api.semanticscholar.org/CorpusID:98411415.

[51] S. Wang, D. Zhang, B. Li, C. Zhang, Z. Du, H. Yin, X. Bi, S. Yang, Ultrastable In-Plane 1T–2H MoS 2 Heterostructures for Enhanced Hydrogen Evolution Reaction, Adv. Energy Mater. 8 (2018). https://doi.org/10.1002/aenm.201801345.

[52] A.P. Grosvenor, B.A. Kobe, M.C. Biesinger, N.S. McIntyre, Investigation of multiplet splitting of Fe 2p XPS spectra and bonding in iron compounds, Surf. Interface Anal. 36 (2004) 1564–1574. https://doi.org/10.1002/sia.1984.

[53] P. Afanasiev, C. Lorentz, Oxidation of Nanodispersed MoS 2 in Ambient Air: The Products and the Mechanistic Steps, J. Phys. Chem. C. 123 (2019) 7486–7494. https://doi.org/10.1021/acs.jpcc.9b01682.

[54] X. Miao, S. Liu, L. Ma, Y. Yang, J. Zhu, Z. Li, J. Wang, Ti3C2-graphene oxide nanocomposite films for lubrication and wear resistance, Tribol. Int. 167 (2022) 107361. https://doi.org/10.1016/j.triboint.2021.107361.

[55] S. Watanabe, J. Noshiro, S. Miyake, Tribological characteristics of WS2/MoS2 solid lubricating multilayer films, Surf. Coatings Technol. 183 (2004) 347–351. https://doi.org/10.1016/j.surfcoat.2003.09.063.

[56] S. Mahathanabodee, T. Palathai, S. Raadnui, R. Tongsri, N. Sombatsompop, Dry sliding wear behavior of SS316L composites containing h-BN and MoS2 solid lubricants, Wear. 316 (2014) 37–48. https://doi.org/10.1016/j.wear.2014.04.015.

[57] M. Chhowalla, G.A.J. Amaratunga, Thin films of fullerene-like MoS2 nanoparticles with ultra-low friction and wear, Nature. 407 (2000) 164–167. https://doi.org/10.1038/35025020.

[58] D. Berman, A. Erdemir, A. V Sumant, Graphene: a new emerging lubricant, Mater. Today. 17 (2014) 31–42. https://doi.org/https://doi.org/10.1016/j.mattod.2013.12.003.

[59] S. Chen, B. Shen, F. Zhang, H. Hong, J. Pan, Mussel-Inspired Graphene Film with Enhanced Durability as a Macroscale Solid Lubricant, ACS Appl. Mater. Interfaces. 11 (2019) 31386–31392. https://doi.org/10.1021/acsami.9b10404.

[60] Y. Liu, J. Li, X. Chen, J. Luo, Fluorinated Graphene: A Promising Macroscale Solid

Lubricant under Various Environments, ACS Appl. Mater. Interfaces. 11 (2019) 40470–40480. https://doi.org/10.1021/acsami.9b13060.

[61] K. Ren, G. Yu, Z. Zhang, W. Wu, P. Tian, M. Chhattal, Z. Gong, Y. Li, J. Zhang, Self-organized transfer film-induced ultralow friction of Graphene/MoWS4 heterostructure nanocomposite, Appl. Surf. Sci. 572 (2022) 151443. https://doi.org/10.1016/j.apsusc.2021.151443.

[62] C. Zishan, L. Hejun, F. Qiangang, Q. Xinfa, Tribological behaviors of SiC/h-BN composite coating at elevated temperatures, Tribol. Int. 56 (2012) 58–65. https://doi.org/10.1016/j.triboint.2012.06.026.

[63] S. Qi, X. Wei, L. Chen, Z. Geng, J. Luo, Z. Lu, G. Zhang, 3D graphene/hexagonal boron nitride composite nanomaterials synergistically reduce the friction and wear of Steel-DLC contacts, Nano Sel. 2 (2021) 791–801. https://doi.org/10.1002/nano.202000233.

[64] D. Dey, S. Sarkar, S. Rawal, A.K. Singh, K.S. Bal, M. Khande, A.K. Nath, A. Roy Choudhury, Correlation of real-time thermal history with tribological properties of laser coated NiCrBSi with Ag and WS2 addition, Surf. Coatings Technol. 431 (2022) 128034. https://doi.org/10.1016/j.surfcoat.2021.128034.

[65] L. Shan, Y. Wang, J. Li, H. Li, X. Wu, J. Chen, Tribological behaviours of PVD TiN and TiCN coatings in artificial seawater, Surf. Coatings Technol. 226 (2013) 40–50. https://doi.org/https://doi.org/10.1016/j.surfcoat.2013.03.034.

[66] J.K. Lancaster, A review of the influence of environmental humidity and water on friction, lubrication and wear, Tribol. Int. 23 (1990) 371–389. https://doi.org/https://doi.org/10.1016/0301-679X(90)90053-R.